

Phonon-Assisted Nonradiative Recombination Tuned by Organic Cations in Ruddlesden-Popper Hybrid Perovskites

Fan Zhang, Xiaolong Wang, Weiwei Gao,^{*} and Jijun Zhao

Key Laboratory of Material Modification by Laser, Ion and Electron Beams (Dalian University of Technology), Ministry of Education, Dalian 116024, China



(Received 29 December 2021; revised 17 May 2022; accepted 19 May 2022; published 8 June 2022)

Significant efforts have been devoted to further increasing the photoconversion efficiency of two-dimensional (2D) organic-inorganic halide perovskites, which are promising photovoltaic materials with superior stability but lower efficiency compared to their three-dimensional counterparts. One of the main factors that limit their photoconversion efficiency is the nonradiative recombination of photoexcited carriers. A widely used strategy for tuning the photoconversion efficiency of 2D perovskites is exchanging various organic cations. However, due to mixed effects contributed to by extrinsic factors, such as defect concentration and sample morphology, experiments alone are insufficient to explain the role of organic cations in phonon-assisted carrier recombination. With time-domain simulations based on first-principles nonadiabatic molecular dynamics, we investigate six prototypical 2D Ruddlesden-Popper perovskites to reveal the impact of organic cations on tuning the nonradiative recombination time through displacing inorganic ions and affecting electron-phonon coupling. The phonon-assisted band-to-band nonradiative recombination time is on the order of a few hundred nanoseconds and can be tuned up to 5 times by modifying organic cations. A distinct correlation between the pure-dephasing time and inorganic atom distortions induced by the motion of organic parts is revealed. Compared to the pure-dephasing time, nonadiabatic coupling (NAC) associated with the strength of electron-phonon coupling plays a more important role in determining the nonradiative carrier recombination time. Notably, fluorinated organic spacers increase the NAC between frontier electronic states and speed up the nonradiative recombination process.

DOI: 10.1103/PhysRevApplied.17.064016

I. INTRODUCTION

Two-dimensional (2D) organic-inorganic halide perovskites (OIHPs) are promising candidates for high-performance photovoltaic applications. They demonstrate many advantages similar to three-dimensional (3D) OIHPs, such as flexible structure, large chemical design space, and high photoconversion efficiency up to 21% [1–5]. In contrast to 3D OIHPs with the general chemical formula AMX_3 , 2D OIHPs have a more complex formula, $A'_m A_{n-1} M_n X_{3n+1}$, where A' represents the organic cation spacer connecting neighboring inorganic sheets, A represents the monovalent organic cation, M represents the divalent metal cation, and X represents the halide anion [6]. Here, n defines the number of $[PbI_6]^{4-}$ sheets between organic cation spacers, while m is set to one or two for Dion-Jacobson- (DJ) or Ruddlesden-Popper- (RP) type perovskites, respectively. The presence of organic cation spacers, A' , in 2D OIHPs is one of the most important factors that separate them from 3D OIHPs. For example,

organic cation spacers create multi-quantum-well structures [7], leading to a much larger exciton-binding energy and faster radiative recombination in 2D OIHPs than that of 3D OIHPs. Additionally, organic cation spacers protect the metal-halide framework from degradation caused by moisture and, as a result, 2D OIHPs demonstrate better environmental stability than 3D OIHPs [2,6]. The wealth of choices for organic cation spacers also enrich the pool of 2D OIHPs and bring more degrees of freedoms for researchers to fine-tune their properties.

Many efforts have been devoted to exploring 2D OIHPs by substituting organic cation spacers, A' , with various monovalent cations, A , and inorganic frameworks [4,8–12]. For instance, experimental and theoretical studies have shown that organic cations A or A' play key roles in changing not only the sample quality, such as defect density, crystallinity, morphology, and environmental stability, but also optoelectronic properties like absorption spectra, optical band gaps, and exciton binding energy [11,13–16]. Consequently, choosing different organic cations has a prominent impact on the performance of the corresponding photovoltaic devices. For example, the photoconversion efficiency of single-junction 2D OIHP devices ranges from

*weiweigao@dlut.edu.cn

4% to more than 21% [5], and organic cations A or A' are usually recognized as the main factor that affects the performance.

In pursuit of better 2D OIHPs for photovoltaic applications, the nonradiative recombination time is a key parameter to be optimized to achieve better photovoltaic performance. Possible nonradiative recombination pathways include Auger recombination, trap-assisted recombination, phonon-assisted band-to-band recombination, and carrier-carrier scattering [17]. The mechanism of how various organic cations change intrinsic properties, such as structural properties, electronic structures, and electron-phonon interactions, which, in turn, determine the nonradiative relaxation times of 2D OIHPs deserve in-depth investigations.

Using density-functional theory (DFT) and nonadiabatic molecular dynamics (NAMD) simulations, herein we comprehensively study the nonradiative recombination processes mediated by electron-phonon interactions in six prototypical 2D OIHPs. We focus on the correlations between the intrinsic properties, such as band-edge states, distortion of crystal structures, and nonradiative relaxation times. Based on the current theory framework, our results demonstrate that direct band-to-band nonradiative recombination is non-negligible and can be adjusted by changing organic cations A or the A' site. A detailed analysis further shows that the motions of organic cations perturb the inorganic framework and lead to various rates of decoherence. We also find that nonadiabatic coupling (NAC) plays a more dominant role than pure-dephasing time in determining the carrier lifetime. A fluorinated organic spacer leads to a larger NAC and faster band-to-band nonradiative recombination.

II. COMPUTATIONAL DETAILS

A first-principles method based on the plane-wave basis and DFT are employed for structural optimization, electronic structure calculations, and *ab initio* molecular dynamics (MD) with the Vienna *ab initio* simulation package (VASP) [18]. Time-dependent *ab initio* NAMD simulations with the decoherence-induced surface-hopping (DISH) technique are carried out using the Hefei-NAMD code [19–22], which augments the VASP. We use the Perdew-Burke-Ernzerhof (PBE) exchange-correlation functional [23]. The DFT-D3 correction [24] is adopted to treat the van der Waals interaction. A plane-wave energy cutoff of 400 eV and a $3 \times 3 \times 1$ Monkhorst-Pack k -point mesh are used for structural relaxations [25]. All structures are optimized until the total energy converges within 10^{-4} eV and the forces are less than 0.01 eV/Å. Cell shapes and cell volumes are allowed to change during geometry optimizations. After geometry optimizations at 0 K, all these structures are heated to 300 K via repeated velocity rescaling using the canonical ensemble (*NVT* ensemble).

Following that, 5-ps adiabatic MD trajectories are generated in the microcanonical ensemble (*NVE* ensemble) with a 1-fs time step. Using the MD trajectory, the NAMD results are computed by averaging over 100 different initial configurations. For each chosen structure, we sample 500 trajectories for 0.5 ns to simulate the nonradiative relaxation process of excited electrons from the conduction-band minimum (CBM) to the valence-band maximum (VBM). Such a band-to-band nonradiative recombination process is caused by the coupling between phonon and electronic states. The NAC between the CBM and VBM is computed using a recently proposed concentric approximation [26]. The frequency and projected density of states of phonon modes are calculated with the PHONOPY package [27–29]. The electron-phonon-coupling matrix elements are computed using a frozen-phonon method using our modified version of Quantum ESPRESSO 7.0 [30].

III. RESULTS AND DISCUSSION

To study the effects of the organic cations A and A' on carrier nonradiative recombination, we consider six representative 2D OIHPs, including $(BA)_2MAPb_2I_7$ [31], its FA-based analogue $(BA)_2FAPb_2I_7$ [32], and its derivatives with different interlayer organic spacers A' , namely, $(HA)_2MAPb_2I_7$ [33], $(PEA)_2MAPb_2I_7$ [2], $(PEA2)_2MAPb_2I_7$ [34], and $(FPEA)_2MAPb_2I_7$ [35] [where acronyms used for organic cations are MA = CH_3NH_3 , FA = $CH(NH_2)_2$, BA = $CH_3(CH_2)_3NH_3$, HA = $CH_3(CH_2)_5NH_3$, PEA = $C_6H_5C_2H_4NH_3$ and FPEA = $C_6H_4FC_2H_4NH_3$]. These six materials are widely investigated by experiments and calculations. They exhibit promising photoconversion efficiencies ranging from 6.82% to 17.3% [35–41]. For clarity, the six perovskites are abbreviated as “BA-MA,” “BA-FA,” “HA-MA,” “PEA-MA,” “PEA2-MA,” and “FPEA-MA” hereafter.

The $2 \times 1 \times 1$ supercell structures of these six systems are depicted in Figs. 1(a)–1(f). Generally speaking, PEA-MA, FPEA-MA, and HA-MA have a longer organic spacer A' than BA-MA. Note that PEA-MA and PEA2-MA are two polymorphs with different arrangements of PEA molecules. PEA-MA has the arrangement with parallel π - π interlayer interactions [Fig. 1(d)], while PEA2-MA has T-shaped π interactions [Fig. 1(e)] [34]. FPEA is obtained by substituting a fluorine atom for the hydrogen atom at the *para* position of the conjugated phenyl ring of PEA cations [Fig. 1(f)] [35]. Table S1 within the Supplemental Material [42] summarizes the optimized lattice constants. The deviation between theoretical lattice parameters and experimental data is less than 2% [31,33,35].

We then investigate the projected density of states (PDOS) of BA-MA, as shown in Fig. 2(a). The other five materials display band-edge states with similar characters, and their PDOS are shown in the Supplemental Material (Fig. S1) [42]. Similar to 3D $MAPbI_3$ perovskite [43],

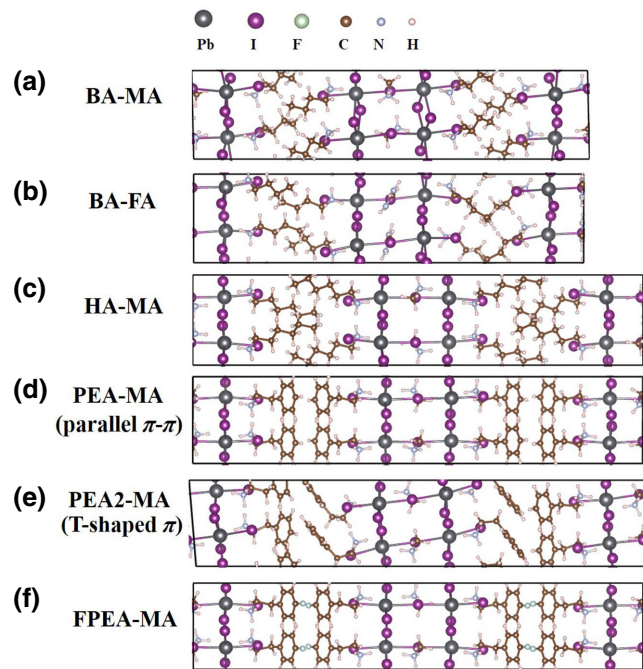


FIG. 1. Optimized structures of (a) BA-MA, (b) BA-FA, (c) HA-MA, (d) PEA-MA, (e) PEA2-MA, and (f) FPEA-MA at 0 K.

the CBM and the VBM are contributed to mainly by Pb and I atoms. Although the organic cations A or A' do not contribute directly to band-edge states, they can indirectly affect the band gap by distorting the inorganic framework, which is also confirmed by previous studies [44–48]. As we will show in the following sections, the distortion of the Pb-I inorganic framework also strongly affects the pure-dephasing time, the nonadiabatic coupling between CBM and VBM, and the nonradiative recombination time.

The electronic band structure of BA-MA is shown in Fig. 2(b). We find that the CBM slightly shifts away from Γ , making the band gap slightly indirect. This originates from the rotations of organic cations that randomly deform the inorganic framework [44,49,50]. Since only scalar-relativistic effects are considered in our calculations, this effect is different from the Rashba-type effect that originates from spin-orbital coupling [51]. Figure 2(c) presents the band gaps of six 2D perovskites and the chemical formulas of different organic cations A and A' . The calculated band gap of BA-MA is 1.86 eV, which is in agreement with a previous DFT calculation [31] and slightly smaller than the experimental value of 1.99 eV [6]. We emphasize that such agreement between the DFT band gap and experimental band gap is largely due to error cancellation of quasiparticle self-energy effects and strong spin-orbital coupling effects [48]. The band gap of FPEA-MA is 1.70 eV, which is smaller than those of PEA-MA (1.77 eV) and PEA2-MA (1.90 eV). Such a calculated trend is in line with a previous experimental report that the optical

gap of the $(4\text{FPEA})_2(\text{MA})_4\text{Pb}_5\text{I}_{16}$ film is slightly redshifted compared to that of $(\text{PEA})_2(\text{MA})_4\text{Pb}_5\text{I}_{16}$ [40].

Notably, during MD simulations, we observe large fluctuations of band gaps, which are caused by significant distortions to the Pb-I frameworks. This is revealed by the distributions of band gaps along the MD trajectories of six 2D OIHPs, as shown in Fig. 2(d). In particular, the range of band-gap fluctuations (i.e., the difference between the smallest and largest band gaps during MD) is around 1 eV. This is much larger than that of inorganic perovskites $\beta\text{-CsPbI}_3$, the range of band gap fluctuation of which is estimated to be around 0.5 eV [52]. We also observe frequent band crossings and order switching among the closely spaced band-edge states, as depicted in Fig. 2(b). Notably, compared to the band gaps calculated using equilibrium structures at 0 K, the average band gaps of the six 2D OIHPs are generally increased, and the differences between the average band gaps also become smaller.

We simulate the time evolution of electron population, $P(t)$, of the CBM for six 2D OIHPs using NAMD, as shown in Fig. 3. Then, the nonradiative-carrier-recombination time, τ , is extrapolated using an exponential decay fitting, $P(t) = e^{-t/\tau} \approx 1 - t/\tau$. Although the trap-assisted process and Auger process are acknowledged to be the dominant nonradiative-recombination processes in 2D OIHP, our study indicates that direct band-to-band recombination is also considerable. As summarized in Table I, the recombination time, τ , ranges from 91 to 440 ns, depending on the organic composition. It is noteworthy that the calculated recombination time becomes smaller if we turn off the concentric approximation [26]. However, the overall trend we discuss here remains the same. When the A site changes from MA to FA in BA-based systems, the calculated τ is more than doubled. This tendency is consistent with the experimental observation that the carrier lifetime increases by 2 orders of magnitude as the composition, x , of FA in $(\text{BA})_2(\text{MA}_{1-x}\text{FA}_x)_3\text{Pb}_4\text{I}_{13}$ increases from 0 to 0.6 [53]. However, doubling of the lifetime, τ , due to FA substitution from the theoretical simulation cannot explain the 2 orders of magnitude increase of lifetime observed in the experiment. This suggests some other extrinsic factors, such as the significant change of sample morphology [53], also play important roles in affecting the nonradiative recombination here.

Examining the effects of interlayer organic spacer A' , we find that the nonradiative-carrier-recombination time generally increases by two- to threefold when we replace BA with a longer organic spacer, such as HA or PEA. In particular, the carrier lifetime of PEA-MA is about twice as large as that of BA-MA. This trend is qualitatively consistent with an earlier theoretical investigation, which found that the carrier lifetime of $(\text{PEA})_2\text{PbI}_4$ was 3 times longer than that of $(\text{BA})_2\text{PbI}_4$ [54]. The numerical discrepancy between our work and Ref. [54] is attributed to the different numbers of $[\text{PbI}_6]^{4-}$ layers and the ways for

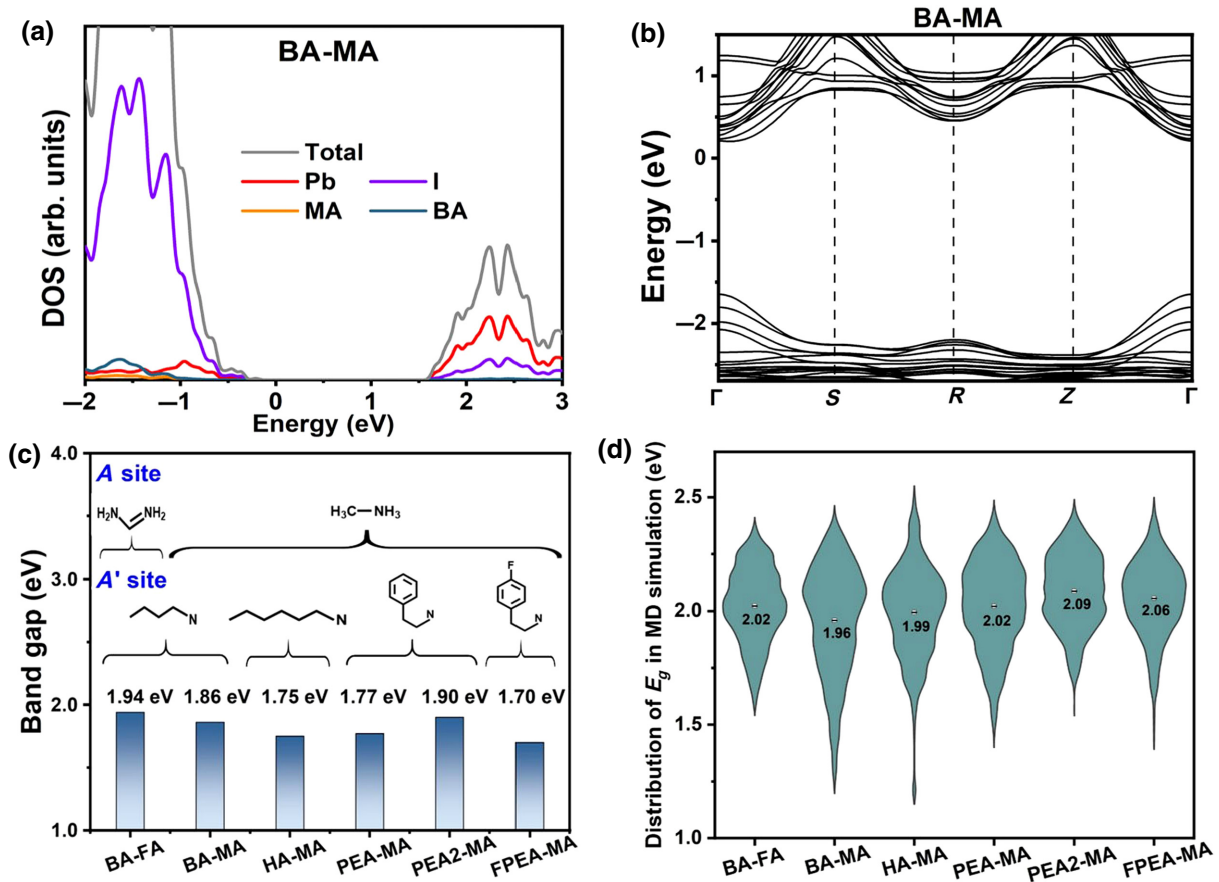


FIG. 2. (a) Total density of states (DOS) and PDOS of BA-MA. (b) Band structures of BA-MA in $2 \times 1 \times 1$ supercell. High-symmetry points along the $\Gamma(0, 0, 0)-S(0, 0, 0.5)-R(0.5, 0, 0.5)-Z(0.5, 0, 0)-\Gamma(0, 0, 0)$ path throughout the Brillouin zone. (c) Band gap calculated with the PBE functional. (d) Distribution of band gaps during 5-ps MD trajectories of six 2D OIHPs. Numbers in the center are average PBE band gaps.

evaluating NAC. When the arrangement of the PEA spacer changes from parallel π - π interlayer interactions (as in PEA-MA) to T-shaped π interactions (as in PEA2-MA), τ shows a relatively small change from 313 to 440 ns. Notably, if one replaces PEA with FPEA, which only differs from PEA by one fluorine atom, the nonradiative-carrier-recombination time decreases significantly.

For a better understanding of the nonradiative-carrier-recombination time, we analyze the band-edge states and structural properties in MD simulations to see how these properties impact two important variables, namely, the pure-dephasing time and NAC. We check the convergence of NAC and dephasing time with MD time, as shown in the Supplemental Material (Fig. S2) [42]. As shown

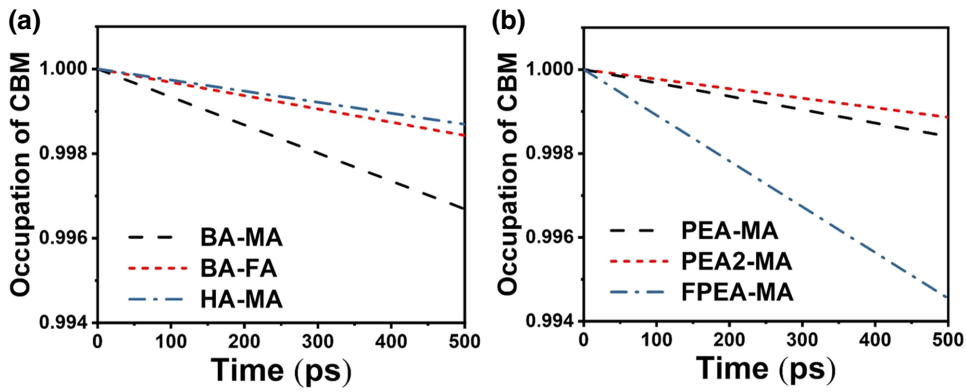


FIG. 3. Electron-hole recombination dynamics in (a) BA-MA, BA-FA, HA-MA, (b) PEA-MA, PEA2-MA, and FPEA-MA.

TABLE I. NACs, pure-dephasing times, and nonradiative-carrier-recombination times for BA-MA, BA-FA, HA-MA, PEA-MA, PEA2-MA and FPEA-MA. The NACs shown here are mean absolute values of non-adiabatic coupling between VBM and CBM.

| | Nonradiative-carrier-recombination time (ns) | NAC (meV) | Pure-dephasing time (fs) |
|---------|--|-----------|--------------------------|
| BA-MA | 151 | 0.187 | 2.81 |
| BA-FA | 318 | 0.178 | 4.12 |
| HA-MA | 382 | 0.168 | 3.24 |
| PEA-MA | 313 | 0.177 | 3.50 |
| PEA2-MA | 440 | 0.156 | 4.22 |
| FPEA-MA | 91.7 | 0.327 | 4.10 |

in Fig. S2 within the Supplemental Material [42], NAC and dephasing time converge well with 5-ps MD simulations. In Figs. 4(a) and 4(b), we present the optical pure-dephasing functions computed using a second-order cumulant approximation [55]:

$$D_{ij}(t) = \exp\left(-\frac{1}{\hbar^2} \int_0^t dt' \int_0^{t'} dt'' C_{ij}(t'')\right), \quad (1)$$

where $C_{ij}(t'')$ is the unnormalized autocorrelation function (UNACF) of the phonon-induced fluctuation of the energy gap, $\delta E_{ij}(t)$, between electronic states i and j , which is defined as

$$C_{ij}(t) = \langle \delta E_{ij}(t') \delta E_{ij}(t+t') \rangle_t. \quad (2)$$

Here, the bracket $\langle \cdot \rangle_t$ denotes calculating the average over MD trajectories, and $\delta E_{ij}(t) = E_{ij}(t) - \langle E_{ij}(t) \rangle_t$. The insets of Figs. 4(a) and 4(b) display the UNACF for fluctuations of the CBM-VBM band gap on similar timescales.

The pure-dephasing times, T , are obtained by fitting $D_{ij}(t)$ to a Gaussian function, $D_{ij}(t) = e^{-0.5(t/T)^2}$, and are summarized in Table I. In general, larger A or A' site organic cations slow down the decoherence process. For instance, substituting MA with heavier FA in BA-based systems raises the pure-dephasing time from 2.81 to 4.12 fs. Similarly, replacing BA with larger inter-layer organic spacers like HA or PEA also increases the pure-dephasing time. The decoherence process is mainly determined by the fluctuation of band gaps during MD simulations [56–58]. Accordingly, we find a clear linear relationship between the pure-dephasing time and the band-gap standard deviation, which is equal to the square root of the initial value of UNACFs, $C_{ij}(0)^{1/2}$. As shown in Fig. 4(c), a smaller band-gap standard deviation leads to a longer pure-dephasing time.

Since the band-edge states are contributed to by the inorganic framework, one may expect a strong correlation between the distortion of the inorganic framework and the band-gap standard deviation. To demonstrate this, we compute the root-mean-squared displacements of lead and iodine ions, $\delta_\alpha = 1/N_\alpha \sum_{i \in \alpha} \sqrt{\langle (\mathbf{r}_i(t) - \langle \mathbf{r}_i(t') \rangle_t)^2 \rangle_t}$, where $\mathbf{r}_i(t)$ indicates the location of atom i of type α ($\alpha = \text{Pb}$ or I) at a given time t , and N_α is the number of atoms of type α . Table II summarizes the root-mean-square displacements in the positions of the lead and iodine ions. We note that changing the A site, by replacing MA with heavier FA, slows down atomic fluctuation and induces smaller displacement of the inorganic framework. Substitution of larger A' -site cations leads to the same trend. Our results in Table II also confirm that iodine atoms move faster than lead atoms because they are lighter. We note that gap standard deviations and root-mean-square displacements of lead and iodine ions also exhibit a prominent positive correlation, as shown in Fig. 4(d). Larger distortion of the inorganic framework leads to larger gap fluctuation and then accelerates decoherence.

Previous studies suggested that longer pure-dephasing times led to shorter nonradiative-recombination times [43,58–61]. For 2D OIHPs, our results reveal a weak correlation between the pure-dephasing time and the carrier-recombination time. Instead, the inverse of NAC, that is d_{jk}^{-1} , exhibits a positive correlation with the nonradiative-recombination time, as displayed in Fig. 5, where d_{jk} represents the NAC between CBM and VBM. This is consistent with the expectation that larger NAC facilitates nonradiative-carrier recombination and reduces the carrier lifetime. In particular, a significantly larger NAC leads to the lowest carrier lifetime in FPEA-MA among six 2D OIHPs. This prediction, however, contradicts a recent experimental finding that $(\text{FPEA})_2(\text{MA})_4\text{Pb}_5\text{I}_{16}$ has a longer carrier lifetime than that of $(\text{PEA})_2(\text{MA})_4\text{Pb}_5\text{I}_{16}$ [40]. The discrepancy is ascribed to the fact that trap-assisted nonradiative recombination also plays an important role here. Experiments reveal that $(\text{FPEA})_2(\text{MA})_4\text{Pb}_5\text{I}_{16}$ samples have a lower trap-state density and higher sample crystallinity than those of $(\text{PEA})_2(\text{MA})_4\text{Pb}_5\text{I}_{16}$ [40]. Accordingly, a higher trap-assisted nonradiative-recombination rate in $(\text{PEA})_2(\text{MA})_4\text{Pb}_5\text{I}_{16}$ samples can counter the advantage of its lower band-to-band nonradiative-recombination rate. If the sample quality, such as defect concentration, can be controlled, one may observe a longer carrier lifetime in $(\text{PEA})_2(\text{MA})_4\text{Pb}_5\text{I}_{16}$ as compared to $(\text{FPEA})_2(\text{MA})_4\text{Pb}_5\text{I}_{16}$.

As previous work argues, the fluorine atom in a FPEA cation creates strong dipole moments, which facilitate the separation of charge carriers [40], so we investigate the real-space charge-density distribution corresponding to the CBM and VBM. We calculate the average charge density,

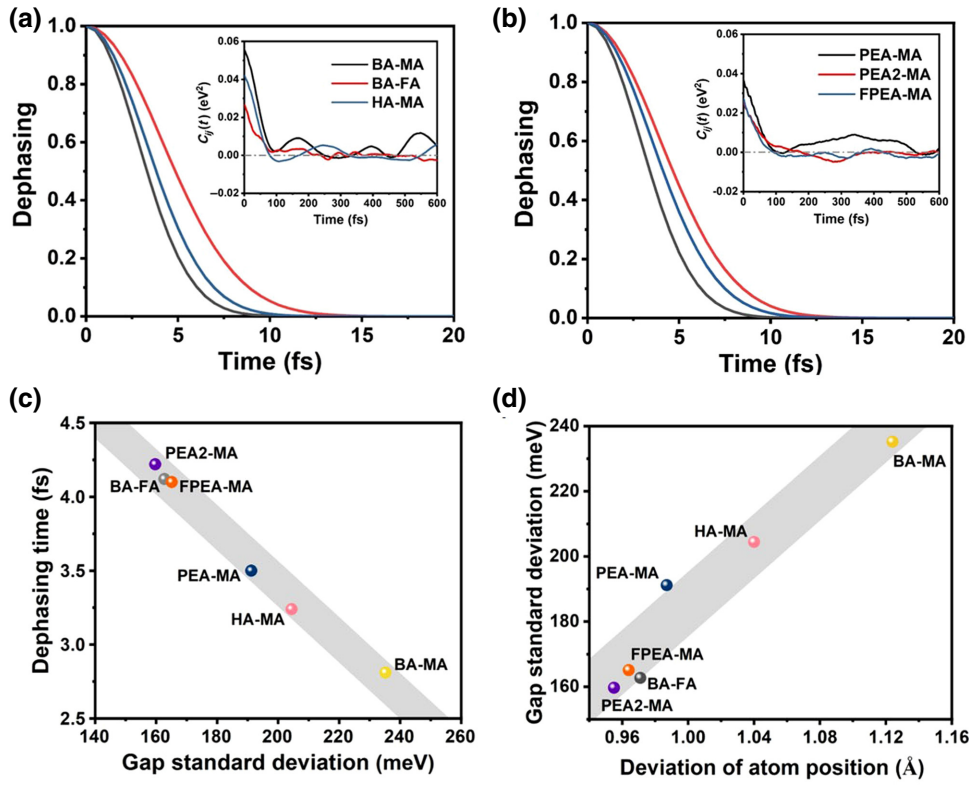


FIG. 4. Pure-dephasing functions for the CBM-VBM transition in (a) BA-MA, BA-FA, and HA-MA and (b) PEA-MA, PEA2-MA, and FPEA-MA. Insets show unnormalized autocorrelation functions of six 2D OIHPs. (c) Pure-dephasing time versus gap standard deviation. Gray area is a guide to the eye. (d) Gap standard-deviation changes versus standard deviation of the positions of Pb and I atoms along 5-ps MD trajectories.

$\langle |\varphi_i(\mathbf{r}, t)|^2 \rangle_t$ (as plotted in Fig. S3 within the Supplemental Material) [42], and compare the overlap between the average charge densities of the VBM and the CBM, $\int \langle |\varphi_{\text{CBM}}(\mathbf{r}, t)|^2 \rangle_t / \langle |\varphi_{\text{VBM}}(\mathbf{r}, t)|^2 \rangle_t d\mathbf{r}$, which are summarized in Table S2 (Supplemental Material) [42]. However, the spatial overlap between these two states only shows small differences and is insufficient to explain the large NAC of FPEA-MA.

To understand the main reason for the distinctively large NAC in FPEA-MA, we further analyze the NAC, which is defined as $d_{jk} = \langle \varphi_j | \partial / \partial t | \varphi_k \rangle$ and here efficiently evaluate it using the following expression combined with a concentric approximation [26]:

$$\left\langle \varphi_j \left| \frac{\partial}{\partial t} \right| \varphi_k \right\rangle = \frac{1}{2\Delta t} [\langle \varphi_j(t) | \varphi_k(t + \Delta t) \rangle - \langle \varphi_j(t + \Delta t) | \varphi_k(t) \rangle]. \quad (3)$$

On the other hand, one can also write $d_{jk} = \dot{\mathbf{R}} \langle \varphi_j | \nabla_{\mathbf{R}} H | \varphi_k \rangle / (\varepsilon_k - \varepsilon_j)$, which suggests that d_{jk} is determined by three factors, namely, nuclear velocity $\dot{\mathbf{R}}$, coupling matrix elements $\langle \varphi_j | \nabla_{\mathbf{R}} H | \varphi_k \rangle$, and energy differences $\varepsilon_k - \varepsilon_j$. The average nuclear velocity, $\dot{\mathbf{R}}$, can be approximately described by the mean atomic displacements of inorganic ions, δ_{Pb} and δ_{I} , which are presented in Table II, and the energy difference can be approximated with the average band gap in Fig. 2(d). Our analysis indicates the mean atomic displacements and average band gap have a weak correlation with NAC between the six systems. As a result, we speculate that a larger $\langle \varphi_j | \nabla_{\mathbf{R}} H | \varphi_k \rangle$ is the dominant factor, which leads to a large NAC and, consequently, a shorter carrier lifetime of FPEA-MA.

The $\langle \varphi_j | \nabla_{\mathbf{R}} H | \varphi_k \rangle$ terms are mainly contributed to by electron-phonon-coupling elements from all phonon modes. To have a deeper understanding of the phonon

TABLE II. Root-mean-square displacements (\AA) of lead and iodine ions for BA-MA, BA-FA, HA-MA, PEA-MA, PEA2-MA, and FPEA-MA.

| | BA-MA | BA-FA | HA-MA | PEA-MA | PEA2-MA | FPEA-MA |
|--|-------|-------|-------|--------|---------|---------|
| δ_{Pb} | 0.543 | 0.467 | 0.466 | 0.437 | 0.417 | 0.445 |
| δ_{I} | 0.581 | 0.504 | 0.574 | 0.550 | 0.538 | 0.519 |
| $\delta_{\text{Pb}} + \delta_{\text{I}}$ | 1.124 | 0.971 | 1.040 | 0.987 | 0.955 | 0.964 |

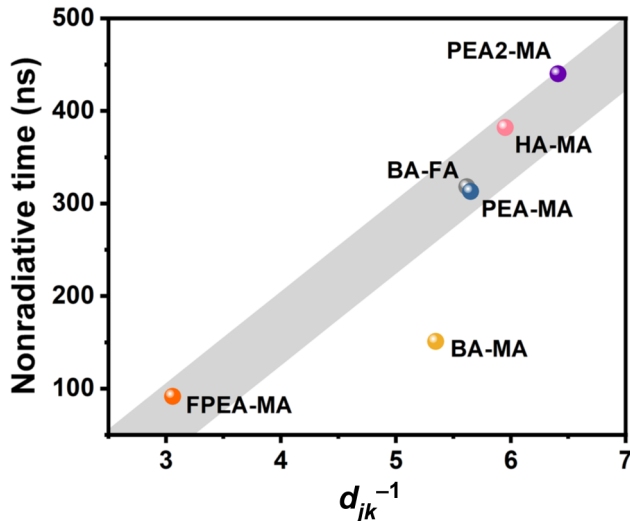


FIG. 5. Nonradiative-recombination time vs d_{jk}^{-1} . Gray area is a guide to the eye.

modes and electron-phonon-coupling strength, we calculate the projected phonon density of states for BA-MA, BA-FA, and FPEA-MA, as shown in Fig. 6(a) and Fig. S4(a) within the Supplemental Material [42]. Our results are similar to the case of 3D perovskites [62]. The low-frequency phonon modes are comprised of the contribution from both $[\text{PbI}_6]^{4-}$ octahedra and organic cations, while the high-frequency modes mainly involve the motion of organic parts. Electron-phonon-coupling matrix elements $g_{mn,v}(k, q)$ are given by

$$g_{mn,v}(\vec{k}, \vec{q}) = \frac{1}{\sqrt{2\omega_{\vec{q}v}}} \left\langle \varphi_{m\vec{k}+\vec{q}} | \Delta_{\vec{q}v} V^{\text{SCF}} | \varphi_{n\vec{k}} \right\rangle, \quad (4)$$

which describe the coupling between the electronic state $|\varphi_{m\vec{k}+\vec{q}}\rangle$ and $|\varphi_{n\vec{k}}\rangle$ through phonon mode v at \vec{q} . Here, $\omega_{\vec{q}v}$ is the phonon-mode frequency, and $\Delta_{\vec{q}v} V^{\text{SCF}}$ is the perturbation of the self-consistent potential subject to a phonon mode. For large supercells of more than 200 atoms, we consider the coupling between the VBM and CBM through zone-center phonon modes, which correspond to $\vec{k} = \vec{q} = \Gamma$. The electron-phonon-coupling matrix element can be evaluated using a frozen-phonon approach [63–65]:

$$g_{mn,v}(\Gamma, \Gamma) = \frac{1}{\sqrt{2\omega_{\Gamma v}}} \times \left\langle \varphi_{m\Gamma} \left| \frac{V^{\text{SCF}}_{[R_0+d\hat{e}_{\Gamma v}]} - V^{\text{SCF}}_{[R_0-d\hat{e}_{\Gamma v}]} }{2d} \right| \varphi_{n\Gamma} \right\rangle, \quad (5)$$

where $V^{\text{SCF}}_{[R_0+d\hat{e}_{\Gamma v}]}$ is the self-consistent potential when the atoms are shifted according to the eigenvector, $\hat{e}_{\Gamma v}$, of

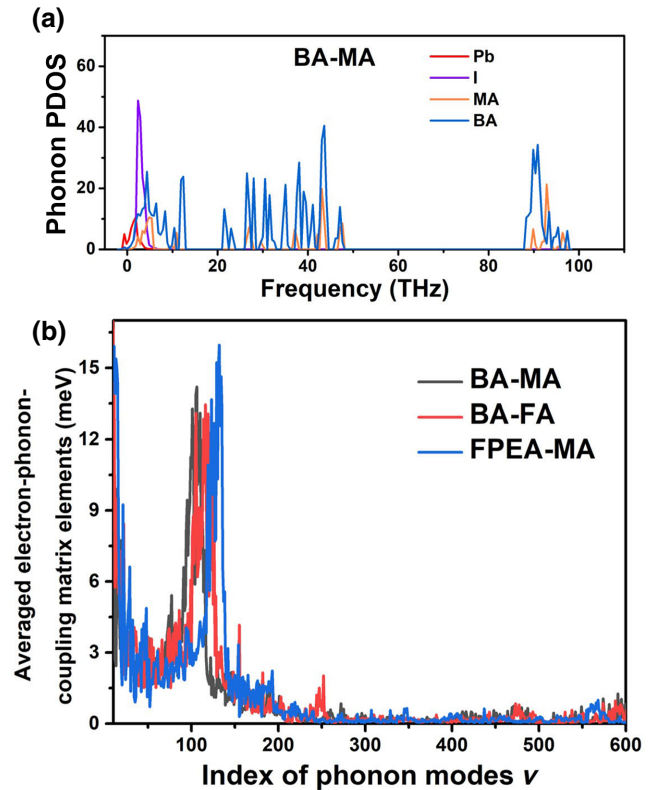


FIG. 6. (a) Projected phonon density of states for BA-MA. (b) Average electron-phonon-coupling matrix elements between the highest four valence states and the lowest nine conduction states at Γ point, for BA-MA, BA-FA, and FPEA-MA.

the phonon mode, v , at Γ . We compute the electron-phonon-coupling matrix element with a small displacement ($d = 0.2$ Bohr). To account for band-reordering effects, the average of the electron-phonon-coupling matrix elements, $\overline{|g_v|}$, between the highest four valence states and the lowest nine conduction states are computed, as shown in Fig. 6(b). The magnitude of the averaged electron-phonon matrix elements, $\overline{|g_v|}$, of FPEA-MA, BA-MA, and BA-FA is large when the phonon frequency, $\omega_{\Gamma v}$, is between 3 and 3.5 THz (see Fig. S4 within the Supplemental Material [42] for results plotted over a wider frequency range), suggesting a strong coupling of band-edge states with low-frequency phonon modes. Notably, the peak of FPEA-MA is 19% and 15% higher than those of BA-MA and BA-FA, respectively. This partially explains a larger NAC of FPEA-MA. We argue that FPEA-MA is a more polarized system and tends to have a stronger Fröhlich coupling constant [66,67]. Although the fluorinated cations, FPEA, do not directly bond with the inorganic framework, the strong electron affinity of fluorine ions makes the charge density more polarized, enhances the interaction between carriers and polar phonons, and results in an overall stronger coupling between frontier electronic states and low-frequency phonon modes.

IV. CONCLUSION

We comprehensively study nonradiative-carrier recombination in six common RP perovskites using first-principles methods. Our results show that the band-to-band nonradiative-recombination time of RP perovskites can be changed by up to fivefold by replacing the organic cations. Although the organic cations do not contribute to the band-edge electronic states, they affect the nonradiative-carrier-recombination process by distorting the inorganic framework and changing the electron-phonon-coupling strength. Large fluctuations of band gaps caused by the distortions of inorganic ions are observed in MD simulations. A distinct positive correlation between pure-dephasing time and inorganic ion displacements is identified. Furthermore, we find that NAC plays a more important role than pure-dephasing time in explaining the nonradiative-recombination time. In particular, a significantly larger NAC in FPEA-MA leads to the lowest carrier lifetime among considered 2D OIHPs. When extrinsic factors like defect concentration and sample morphology can be controlled, one should avoid fluorinated organic cations to achieve longer nonradiative-recombination times. Further analysis shows that the electron-phonon-coupling elements between the VBM and CBM states in FPEA-MA are stronger than those of BA-MA and BA-FA.

ACKNOWLEDGMENTS

This work is supported by the National Natural Science Foundation of China (Grants No. 12104080 and No. 91961204); the Fundamental Research Funds for the Central Universities (Grant No. DUT21RC(3)033); and the XingLiaoYingCai Project of Liaoning province, China (Grant No. XLYC1905014). The authors acknowledge use of the computer resources provided by the Supercomputing Center of Dalian University of Technology and the Shanghai Supercomputer Center.

- [1] N. J. Jeon, J. H. Noh, Y. C. Kim, W. S. Yang, S. Ryu, and S. I. Seok, Solvent engineering for high-performance inorganic–organic hybrid perovskite solar cells, *Nat. Mater.* **13**, 897 (2014).
- [2] I. C. Smith, E. T. Hoke, D. Solis-Ibarra, M. D. McGehee, and H. I. Karunadasa, A layered hybrid perovskite solar-cell absorber with enhanced moisture stability, *Angew. Chem., Int. Ed.* **53**, 11232 (2014).
- [3] E. Shi, Y. Gao, B. P. Finkenauer, A. Akriti, A. H. Coffey, and L. Dou, Two-dimensional halide perovskite nanomaterials and heterostructures, *Chem. Soc. Rev.* **47**, 6046 (2018).
- [4] L. Mao, C. C. Stoumpos, and M. G. Kanatzidis, Two-dimensional hybrid halide perovskites: Principles and promises, *J. Am. Chem. Soc.* **141**, 1171 (2019).

- [5] M. Shao, T. Bie, L. Yang, Y. Gao, X. Jin, F. He, N. Zheng, Y. Yu, and X. Zhang, Over 21% efficiency stable 2D perovskite solar cells, *Adv. Mater.* **34**, 2107211 (2022).
- [6] D. H. Cao, C. C. Stoumpos, O. K. Farha, J. T. Hupp, and M. G. Kanatzidis, 2D homologous perovskites as light-absorbing materials for solar cell applications, *J. Am. Chem. Soc.* **137**, 7843 (2015).
- [7] T. He, S. Li, Y. Jiang, C. Qin, M. Cui, L. Qiao, H. Xu, J. Yang, R. Long, H. Wang, and M. Yuan, Reduced-dimensional perovskite photovoltaics with homogeneous energy landscape, *Nat. Commun.* **11**, 1672 (2020).
- [8] J. Liu, J. Leng, K. Wu, J. Zhang, and S. Jin, Observation of internal photoinduced electron and hole separation in hybrid two-dimensional perovskite films, *J. Am. Chem. Soc.* **139**, 1432 (2017).
- [9] T. M. Koh, V. Shanmugam, J. Schlipf, L. Oesinghaus, P. Müller-Buschbaum, N. Ramakrishnan, V. Swamy, N. Mathews, P. P. Boix, and S. G. Mhaisalkar, Nanostructuring mixed-dimensional perovskites: A route toward tunable, efficient photovoltaics, *Adv. Mater.* **28**, 3653 (2016).
- [10] Y. Chen, Y. Sun, J. Peng, W. Zhang, X. Su, K. Zheng, T. Pullerits, and Z. Liang, Tailoring organic cation of 2D air-stable organometal halide perovskites for highly efficient planar solar cells, *Adv. Energy Mater.* **7**, 1700162 (2017).
- [11] M. Kim, G. H. Kim, T. K. Lee, I. W. Choi, H. W. Choi, Y. Jo, Y. J. Yoon, J. W. Kim, J. Lee, D. Huh, H. Lee, S. K. Kwak, J. Y. Kim, and D. S. Kim, Methylammonium chloride induces intermediate phase stabilization for efficient perovskite solar cells, *Joule* **3**, 2179 (2019).
- [12] X. Jiang, F. Wang, Q. Wei, H. Li, Y. Shang, W. Zhou, C. Wang, P. Cheng, Q. Chen, L. Chen, and Z. Ning, Ultra-high open-circuit voltage of tin perovskite solar cells via an electron transporting layer design, *Nat. Commun.* **11**, 1245 (2020).
- [13] D. Lu, G. Lv, Z. Xu, Y. Dong, X. Ji, and Y. Liu, Thiophene-based two-dimensional Dion-Jacobson perovskite solar cells with over 15% efficiency, *J. Am. Chem. Soc.* **142**, 11114 (2020).
- [14] C. C. Stoumpos, C. M. M. Soe, H. Tsai, W. Nie, J.-C. Blancon, D. H. Cao, F. Liu, B. Traoré, C. Katan, J. Even, A. D. Mohite, and M. G. Kanatzidis, High members of the 2D Ruddlesden-Popper halide perovskites: Synthesis, optical properties, and solar cells of $(\text{CH}_3(\text{CH}_2)_3\text{NH}_3)_2(\text{CH}_3\text{NH}_3)_4\text{Pb}_5\text{I}_{16}$, *Chem* **2**, 427 (2017).
- [15] E. S. Vasileiadou, B. Wang, I. Spanopoulos, I. Hadar, A. Navrotsky, and M. G. Kanatzidis, Insight on the stability of thick layers in 2D Ruddlesden-Popper and Dion-Jacobson lead iodide perovskites, *J. Am. Chem. Soc.* **143**, 2523 (2021).
- [16] S. C. M. Myae, G. P. Nagabhushana, S. Radha, T. Hsinhan, N. Wanyi, B. Jean-Christophe, M. Ferdinand, D. H. Cao, T. Boubacar, P. Laurent, K. Mikaël, K. Claudine, E. Jacky, T. J. Marks, N. Alexandra, A. D. Mohite, C. C. Stoumpos, and M. G. Kanatzidis, Structural and thermodynamic limits of layer thickness in 2D halide perovskites, *Proc. Natl. Acad. Sci.* **116**, 58 (2019).
- [17] L. M. Pazos-Outón, T. P. Xiao, and E. Yablonovitch, Fundamental efficiency limit of lead iodide perovskite solar cells, *J. Phys. Chem. Lett.* **9**, 1703 (2018).

- [18] G. Kresse and J. Furthmüller, Efficient iterative schemes for ab initio total-energy calculations using a plane-wave basis set, *Phys. Rev. B* **54**, 11169 (1996).
- [19] Q. Zheng, W. Chu, C. Zhao, L. Zhang, H. Guo, Y. Wang, X. Jiang, and J. Zhao, Ab initio nonadiabatic molecular dynamics investigations on the excited carriers in condensed matter systems, *Wiley Interdiscip. Rev.: Comput. Mol. Sci.* **9**, e1411 (2019).
- [20] H. M. Jaeger, S. Fischer, and O. V. Prezhdo, Decoherence-induced surface hopping, *J. Chem. Phys.* **137**, 22A545 (2012).
- [21] C. F. Craig, W. R. Duncan, and O. V. Prezhdo, Trajectory Surface Hopping in the Time-Dependent Kohn-Sham Approach for Electron-Nuclear Dynamics, *Phys. Rev. Lett.* **95**, 163001 (2005).
- [22] A. V. Akimov and O. V. Prezhdo, Advanced capabilities of the PYXAID program: Integration schemes, decoherence effects, multiexcitonic states, and field-matter interaction, *J. Chem. Theory Comput.* **10**, 789 (2014).
- [23] J. P. Perdew, K. Burke, and M. Ernzerhof, Generalized Gradient Approximation Made Simple, *Phys. Rev. Lett.* **77**, 3865 (1996).
- [24] S. Grimme, Semiempirical GGA-type density functional constructed with a long-range dispersion correction, *J. Comput. Chem.* **27**, 1787 (2006).
- [25] H. J. Monkhorst and J. D. Pack, Special points for Brillouin-zone integrations, *Phys. Rev. B* **13**, 5188 (1976).
- [26] W. Chu and O. V. Prezhdo, Concentric approximation for fast and accurate numerical evaluation of nonadiabatic coupling with projector augmented-wave pseudopotentials, *J. Phys. Chem. Lett.* **12**, 3082 (2021).
- [27] A. Togo, L. Chaput, and I. Tanaka, Distributions of phonon lifetimes in Brillouin zones, *Phys. Rev. B* **91**, 94306 (2015).
- [28] J. M. Skelton, S. C. Parker, A. Togo, I. Tanaka, and A. Walsh, Thermal physics of the lead chalcogenides PbS, PbSe, and PbTe from first principles, *Phys. Rev. B* **89**, 205203 (2014).
- [29] A. Togo, L. Chaput, I. Tanaka, and G. Hug, First-principles phonon calculations of thermal expansion in Ti_3SiC_2 , $TiAlC_2$, and Ti_3GeC_2 , *Phys. Rev. B* **81**, 174301 (2010).
- [30] P. Giannozzi, *et al.*, QUANTUM ESPRESSO: A modular and open-source software project for quantum simulations of materials, *J. Phys. Condens. Matter* **21**, 395502 (2009).
- [31] C. C. Stoumpos, D. H. Cao, D. J. Clark, J. Young, J. M. Rondinelli, J. I. Jang, J. T. Hupp, and M. G. Kanatzidis, Ruddlesden-Popper hybrid lead iodide perovskite 2D homologous semiconductors, *Chem. Mater.* **28**, 2852 (2016).
- [32] C. Lan, G. Liang, S. Zhao, B. Fan, H. Lan, H. Peng, H. Sun, D. Zhang, J. Luo, and P. Fan, Structural and optical properties of 2D Ruddlesden-Popper perovskite $(BA)_2(FA)_n \cdot 1PbI_3n + 1$ compounds for photovoltaic applications, *J. Am. Ceram. Soc.* **102**, 4152 (2019).
- [33] Y. Fu, M. P. Hautzinger, Z. Luo, F. Wang, D. Pan, M. M. Aristov, I. A. Guzei, A. Pan, X. Zhu, and S. Jin, Incorporating large A cations into lead iodide perovskite cages: Relaxed Goldschmidt tolerance factor and impact on exciton-phonon interaction, *ACS Cent. Sci.* **5**, 1377 (2019).
- [34] M. A. Reyes-Martinez, P. Tan, A. Kakekhani, S. Banerjee, A. A. Zhumeenov, W. Peng, O. M. Bakr, A. M. Rappe, and Y. L. Loo, Unraveling the elastic properties of (quasi)two-dimensional hybrid perovskites: A joint experimental and theoretical study, *ACS Appl. Mater. Interfaces* **12**, 17881 (2020).
- [35] A. H. Slavney, R. W. Smaha, I. C. Smith, A. Jaffe, D. Umeyama, and H. I. Karunadasa, Chemical approaches to addressing the instability and toxicity of lead-halide perovskite absorbers, *Inorg. Chem.* **56**, 46 (2017).
- [36] H. Tsai, W. Nie, J.-C. Blancon, C. C. Stoumpos, R. Asadpour, B. Harutyunyan, A. J. Neukirch, R. Verduzco, J. J. Crochet, S. Tretiak, L. Pedesseau, J. Even, M. A. Alam, G. Gupta, J. Lou, P. M. Ajayan, M. J. Bedzyk, M. G. Kanatzidis, and A. D. Mohite, High-efficiency two-dimensional Ruddlesden-Popper perovskite solar cells, *Nature* **536**, 312 (2016).
- [37] F. Zhang, D. H. Kim, H. Lu, J. S. Park, B. W. Larson, J. Hu, L. Gao, C. Xiao, O. G. Reid, X. Chen, Q. Zhao, P. F. Ndione, J. J. Berry, W. You, A. Walsh, M. C. Beard, and K. Zhu, Enhanced charge transport in 2D perovskites via fluorination of organic cation, *J. Am. Chem. Soc.* **141**, 5972 (2019).
- [38] X. Zhang, G. Wu, S. Yang, W. Fu, Z. Zhang, C. Chen, W. Liu, J. Yan, W. Yang, and H. Chen, Vertically oriented 2D layered perovskite solar cells with enhanced efficiency and good stability, *Small* **13**, 1700611 (2017).
- [39] Y. Hao, Z. Qiu, X. Zhang, Z. Wei, J. Yao, and H. Cai, Series of 2D multilayered perovskites constructed by slicing the 3D $[(CH_3NH_3)PbI_3]$ with 4-fluorobenzylamine, *Inorg. Chem. Commun.* **97**, 134 (2018).
- [40] J. Shi, Y. Gao, X. Gao, Y. Zhang, J. Zhang, X. Jing, and M. Shao, Fluorinated low-dimensional Ruddlesden-Popper perovskite solar cells with over 17% power conversion efficiency and improved stability, *Adv. Mater.* **31**, 1901673 (2019).
- [41] W. Fu, H. Liu, X. Shi, L. Zuo, X. Li, and A. K.-Y. Jen, Tailoring the functionality of organic spacer cations for efficient and stable quasi-2D perovskite solar cells, *Adv. Funct. Mater.* **29**, 1900221 (2019).
- [42] See the Supplemental Material at <http://link.aps.org/supplemental/10.1103/PhysRevApplied.17.064016> for density of states, the convergence of NAC and dephasing time, CBM and VBM average charge densities, electron-phonon coupling matrix elements, and optimized lattice constants in six 2D OIHPs.
- [43] R. Shi and R. Long, Hole localization inhibits charge recombination in tin-lead mixed perovskites: Time-domain ab initio analysis, *J. Phys. Chem. Lett.* **10**, 6604 (2019).
- [44] C. Motta, F. El-Mellouhi, S. Kais, N. Tabet, F. Alharbi, and S. Sanvito, Revealing the role of organic cations in hybrid halide perovskite $CH_3NH_3PbI_3$, *Nat. Commun.* **6**, 7026 (2015).
- [45] S. Maheshwari, S. Patwardhan, G. C. Schatz, N. Renaud, and F. C. Grozema, The effect of the magnitude and direction of the dipoles of organic cations on the electronic

- structure of hybrid halide perovskites, *Phys. Chem. Chem. Phys.* **21**, 16564 (2019).
- [46] M. G. Ju, M. Chen, Y. Zhou, H. F. Garces, J. Dai, L. Ma, N. P. Padture, and X. C. Zeng, Earth-abundant nontoxic titanium(IV)-based vacancy-ordered double perovskite halides with tunable 1.0 to 1.8 eV bandgaps for photovoltaic applications, *ACS Energy Lett.* **3**, 297 (2018).
- [47] Q. Xu, A. Stroppa, J. Lv, X. Zhao, D. Yang, K. Biswas, and L. Zhang, Impact of organic molecule rotation on the optoelectronic properties of hybrid halide perovskites, *Phys. Rev. Mater.* **3**, 125401 (2019).
- [48] W. Gao, X. Gao, T. A. Abtew, Y. Sun, S. Zhang, and P. Zhang, Quasiparticle band gap of organic-inorganic hybrid perovskites: Crystal structure, spin-orbit coupling, and self-energy effects, *Phys. Rev. B* **93**, 85202 (2016).
- [49] X. Zhang, M. Zhang, and G. Lu, Charge stripe formation in molecular ferroelectric organohalide perovskites for efficient charge separation, *J. Phys. Chem. C* **120**, 23969 (2016).
- [50] N. Pandech, T. Kongnok, N. Palakawong, S. Limpijumnong, W. R. L. Lambrecht, and S. Jungthawan, Effects of the van der Waals interactions on structural and electronic properties of $\text{CH}_3\text{NH}_3(\text{Pb}, \text{Sn})(\text{I}, \text{Br}, \text{Cl})_3$ halide perovskites, *ACS Omega* **5**, 25723 (2020).
- [51] D. Ghosh, A. R. Smith, A. B. Walker, and M. S. Islam, Mixed A-cation perovskites for solar cells: Atomic-scale insights into structural distortion, hydrogen bonding, and electronic properties, *Chem. Mater.* **30**, 5194 (2018).
- [52] W. Chu, W. A. Saidi, J. Zhao, and O. V. Prezhdo, Soft lattice and defect covalency rationalize tolerance of β -CsPbI₃ perovskite solar cells to native defects, *Angew. Chemie Int. Ed.* **59**, 6435 (2020).
- [53] N. Zhou, Y. Shen, L. Li, S. Tan, N. Liu, G. Zheng, Q. Chen, and H. Zhou, Exploration of crystallization kinetics in quasi two-dimensional perovskite and high performance solar cells, *J. Am. Chem. Soc.* **140**, 459 (2018).
- [54] D. Ghosh, D. Acharya, L. Pedesseau, C. Katan, J. Even, S. Tretiak, and A. J. Neukirch, Charge carrier dynamics in two-dimensional hybrid perovskites: Dion-Jacobson vs. Ruddlesden-Popper phases, *J. Mater. Chem. A* **8**, 22009 (2020).
- [55] S. Mukamel, *Principles of Nonlinear Optical Spectroscopy* (Oxford University Press, New York, 1995).
- [56] A. B. Madrid, K. Hyeon-Deuk, B. F. Habenicht, and O. V. Prezhdo, Phonon-induced dephasing of excitons in semiconductor quantum dots: Multiple exciton generation, fission, and luminescence, *ACS Nano* **3**, 2487 (2009).
- [57] A. V. Akimov and O. V. Prezhdo, Persistent electronic coherence despite rapid loss of electron–nuclear correlation, *J. Phys. Chem. Lett.* **4**, 3857 (2013).
- [58] J. He, W. H. Fang, R. Long, and O. V. Prezhdo, Increased lattice stiffness suppresses nonradiative charge recombination in MAPbI₃ doped with larger cations: Time-domain ab initio analysis, *ACS Energy Lett.* **3**, 2070 (2018).
- [59] J. He, A. S. Vasenko, R. Long, and O. V. Prezhdo, Halide composition controls electron-hole recombination in cesium-lead halide perovskite quantum dots: A time domain ab initio study, *J. Phys. Chem. Lett.* **9**, 1872 (2018).
- [60] X. Yu, Y. Su, W. W. Xu, and J. Zhao, Efficient photoexcited charge separation at the interface of a novel 0D/2D heterojunction: A time-dependent ultrafast dynamic study, *J. Phys. Chem. Lett.* **12**, 2312 (2021).
- [61] J. Su, Q. Zheng, Y. Shi, and J. Zhao, Interlayer polarization explains slow charge recombination in two-dimensional halide perovskites by nonadiabatic molecular dynamics simulation, *J. Phys. Chem. Lett.* **11**, 9032 (2020).
- [62] F. Brivio, J. M. Frost, J. M. Skelton, A. J. Jackson, O. J. Weber, M. T. Weller, A. R. Goñi, A. M. A. Leguy, P. R. F. Barnes, and A. Walsh, Lattice dynamics and vibrational spectra of the orthorhombic, tetragonal, and cubic phases of methylammonium lead iodide, *Phys. Rev. B* **92**, 144308 (2015).
- [63] K. J. Chang and M. L. Cohen, Electron-phonon interactions and superconductivity in Si, Ge, and Sn, *Phys. Rev. B* **34**, 4552 (1986).
- [64] P. K. Lam, M. M. Dacorogna, and M. L. Cohen, Self-consistent calculation of electron-phonon couplings, *Phys. Rev. B* **34**, 5065 (1986).
- [65] F. Giustino, Electron-phonon interactions from first principles, *Rev. Mod. Phys.* **89**, 15003 (2017).
- [66] H. Fröhlich, H. Pelzer, and S. Zienau, XX. Properties of slow electrons in polar materials, *London, Edinburgh, Dublin Philos. Mag. J. Sci.* **41**, 221 (1950).
- [67] C. Franchini, M. Reticcioli, M. Setvin, and U. Diebold, Polarons in materials, *Nat. Rev. Mater.* **6**, 560 (2021).